INL/CON-08-13992
PREPRINT

3D CFD Electrochemical and Heat Transfer Model of an Integrated-Planar Solid Oxide Electrolysis Cells

IMECE 2008

Grant Hawkes
James O'Brien

October 2008

The INL is a
U.S. Department of Energy
National Laboratory
operated by
Battelle Energy Alliance

2008 ASME International Mechanical Engineering Congress and Exposition
IMECE2008
Oct 31 – Nov 6, 2008, Boston, Massachusetts, USA

IMECE2008-68866

3D CFD ELECTROCHEMICAL AND HEAT TRANSFER MODEL OF AN INTEGRATED-PLANAR SOLID OXIDE ELECTROLYSIS CELLS

Grant Hawkes
Idaho National Laboratory
Idaho Falls, Idaho, USA

James O'Brien
Idaho National Laboratory
Idaho Falls, Idaho, USA

ABSTRACT

A three-dimensional computational fluid dynamics (CFD) electrochemical model has been created to assess high-temperature electrolysis performance of an Integrated Planar porous-tube-supported Solid Oxide Electrolysis Cell (IP-SOEC). The model includes ten integrated planar cells in a segmented-in-series geometry deposited on a flattened ceramic support tube. Mass, momentum, energy, and species conservation and transport are provided via the core features of the commercial CFD code FLUENT. A solid-oxide fuel cell (SOFC) module adds the electrochemical reactions and loss mechanisms and computation of the electric field throughout the cell. The FLUENT SOFC user-defined subroutine was modified for this work to allow for operation in the SOEC mode. Model results provide detailed profiles of temperature, Nernst potential, operating potential, activation over-potential, anode-side gas composition, cathode-side gas composition, current density and hydrogen production over a range of stack operating conditions. Predicted mean outlet hydrogen and steam concentrations vary linearly with current density, as expected. Contour plots of local electrolyte temperature, current density, and Nernst potential indicated the effects of heat transfer, endothermic reaction, Ohmic heating, and change in local gas composition.

Results are discussed for using this design in the electrolysis mode. Discussion of thermal neutral voltage, enthalpy of reaction, hydrogen production is reported herein. Predictions show negative pressure in the H_2 electrode, indicating a possible limit of H_2O diffusion through the ceramic tube. Minimum temperatures occur in the fuel and air downstream corner of the ceramic tube for voltages below the thermal neutral point.

INTRODUCTION

A research program is under way at the Idaho National Laboratory (INL) to simultaneously address the research and scale-up issues associated with the implementation of high-temperature electrolysis for large-scale hydrogen production from nuclear energy [1,2]. The research program includes an experimental and modeling program aimed at performance characterization of electrolysis cells and stacks. Stacks of electrolysis cells [3] have been analyzed in showing the importance of flow distribution through large planar stacks. Previous models [4] also include single-cell planar cross flow designs. The INL research program also includes materials development tasks. This paper is focused on consideration of the Integrated Planar Solid Oxide Electrolysis Cell (IP-SOEC) design [5]. A typical IP-SOEC consists of a flattened ceramic tube with segmented-in-series electrochemical cells deposited on its outer surfaces. This design concept represents a cross between tubular and planar fuel cell designs. In the electrolysis mode, a steam/hydrogen gas mixture is supplied to the hydrogen electrode from interior flow channels. Hydrogen diffuses from the internal flow channels to the hydrogen electrodes through the porous tube structure. Air flows over the outside of the tubes.

For detailed SOEC modeling, the commercial CFD code FLUENT was selected. Fluent Inc. was funded by the US Department of Energy National Energy Technology Laboratory (DOE-NETL) to develop a solid-oxide fuel cell (SOFC) module for coupling to the core mass, momentum, energy, and species conservation and transport features of the FLUENT CFD code. The SOFC module adds the electrochemical reactions and loss mechanisms and computation of the electric field throughout the cell. The FLUENT SOFC user-defined subroutine was modified for this work to allow for operation in the SOEC mode. Model results provide detailed profiles of temperature, Nernst potential, operating potential, anode-side gas composition, cathode-side gas composition, current density and hydrogen production over a range of stack operating conditions.

NOMENCLATURE

c_p	specific heat (J/kg-K)
d_p	pore diameter
F	Faraday constant (96487 J/V-mol)
h	thickness
H_R	enthalpy of reaction (J/mol)
i	current density
i_o	exchange current density
j	number of electrons passed per reaction (2)
k_i	physical permeability (m^2)
I	cell current
$\dot{m}$	mass flow rate (kg/s)
N	molar flow rate (mol/s)
p	absolute pressure
Q	external heat
R	radius of particles
R_u	universal gas constant (J/kg-K)
T	temperature
V	voltage
W	work (V*I) (Watts)
X_i	mole fraction of component i
ε	porosity
γ	stoichiometric exponent
μ	molecular viscosity (kg/m-s)
σ_e	electronic conductivity (S/m)
σ_i	ionic conductivity (S/m)
τ	tortuosity

NUMERICAL MODEL

A single half-tube model was considered in this study, as shown in Figure 1. The tube has 15 internal flow channels and ten cells printed on its outer surface. Adiabatic symmetry boundaries are assumed on the top and bottom of the domain highlighted by broken lines in Figure 1.

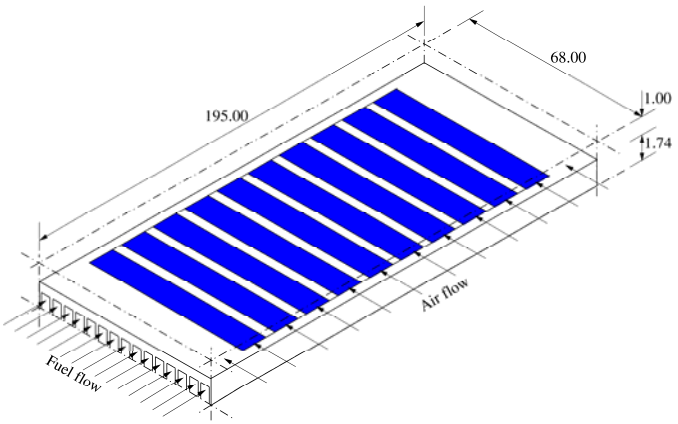

Figure 1. Single half-height tube model (dimensions in mm).

A steam/hydrogen mixture is introduced directly into the 15 internal flow channels as a mass-flow boundary condition at the lower left in Figure 1. Air is introduced in cross-flow as a mass-flow boundary condition at the lower right. The air flow region extends 1.0 mm above the cells, representing half of the distance to the adjacent tube within a possible stack design. A cross-sectional view of the cell geometry is shown in Figure 2, based on typical public-domain data for a row of segmented-in-series cells [6].

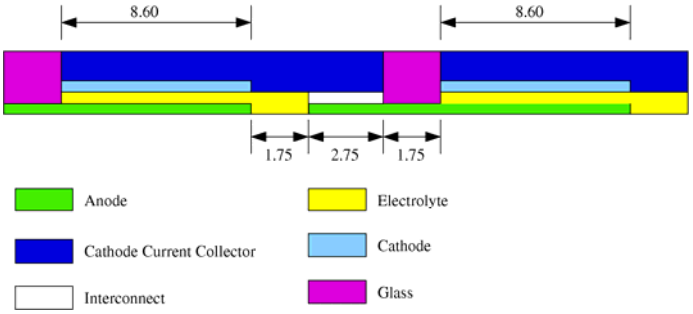

Figure 2. IP-SOFC cell layout and dimensions in mm.

Table 1. IP-SOFC dimensions and properties.

Property	Tube Wall	Anode	Electrolyte	Cathode	CCC
Composition	Common Tile	YSZ-Ni	YSZ	YSZ-LSM	LSM
Porosity, ε	0.2	0.2	0	0.2	0.2
Tortuosity, β	2	2	0	2	2
Pore diameter, d_p (μm)	3	1	0	1	1
Thickness, h (μm)	800	30	20	30	175
Thermal conductivity, k (W/m·K)	5	5	5	5	5
Electrical conductivity σ_e(S/cm)	-	700	-	25	50
Ionic conductivity σ_i(S/cm)	-	-	0.14	-	-
Exchange current density, i_o (A/m^2)	-	5300	-	2000	-

The numerical grid for the first cell is displayed in Figure 3. Previous experience by the author [3] has indicated that three numerical grid cells through the thickness of the electrodes are sufficient to yield very good results. The numerical grid regions shown in Figure 3 indicate the internal flow channels, ceramic tube support, H_2 current collector, H_2 electrode, electrolyte, O_2 electrode, O_2 current collector, and air, respectively, from bottom to top. Each cell includes the anode, electrolyte and cathode layers and an additional layer, the O_2 current collector, which is used to increase the electrical conductivity of the air side of the cells [6]. The relevant properties of these cell components and the supporting tube are listed in Table 1 [6, 7]. Constant exchange current densities i_0 have been specified to facilitate straightforward comparisons between models. A detailed description of the FLUENT SOFC module can be found in Ref [4]. The electrolyte in FLUENThas zero thickness and is treated as a 2-D surface with mass sources and sinks provided to the nearby electrodes.

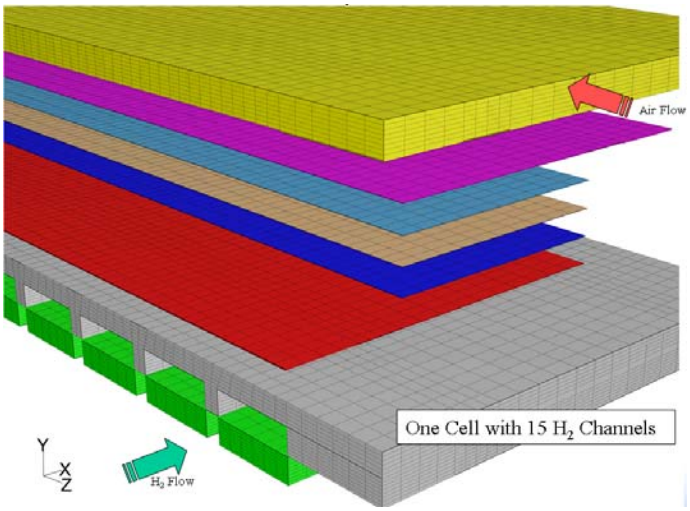

Figure 3. Mesh of single cell with layers.

The prescribed temperature boundary condition at the steam/hydrogen and air flow inlets is 1173 K. Mole fraction inlet compositions are 10% hydrogen and 90% steam in the fuel channels and 21% oxygen, 79% nitrogen on the air side. Hydrogen is necessary to remain under reducing conditions. Total inlet mass flow rates of 3.54 x 10^{-5} kg/s and 2.67 x 10^{-4} kg/s are specified for the steam/hydrogen and air flow inlets, respectively. Outlet pressures of 1 bar are prescribed for both outlet flows. The overall steam utilization for an individual IP-SOFC tube (consisting of 10 electrolysis cells) is quite low, only around 4.0% for a nominal operating current of 1.5 A. Within a stack the complete fuel flow path includes several tubes connected in series, so that the utilization for an entire bundle would be relatively high around 90%.

Permeability for the ceramic tube, electrodes, and current collectors was calculated using the following equation from Ref [8] as:

$$K_i(T) = \left[\frac{R\,p}{8\mu_i(T)} + \frac{2}{3}\left(\frac{8R_uT}{\pi X_i}\right)^{1/2} \right] \frac{R\varepsilon}{\tau^2} \tag{1}$$

where K_i has units of m^2/s. To convert to physical permeability with units of m^2,

$$k_i = K_i \frac{\mu_i}{p} \tag{2}$$

where typical values of k_i in the ceramic substrate are 5.0 x 10^{-14} m^2. The activation overpotential in FLUENT is treated with an effective exchange current density where

$$i_{0eff} = i_{0,ref} (X_i)^{\gamma} \tag{3}$$

The FLUENT input in the activation panel is for $i_{0,ref}$. Previous work by the authors [9] compares several SOFC code results to this same geometry in. In order to compare results, the activation overpotential needed to be comparable between codes. This was accomplished by setting γ equal to zero, so that $i_{0eff}=i_{0,ref}$, where i_{0eff} is used to calculate the activation overpotential for the cathode and anode by:

$$V_{act} = \frac{2R_uT}{jF} \sinh^{-1}\left(\frac{i}{i_{0eff}}\right) \tag{4}$$

In the electrolysis mode, the net heat flux is negative at low current densities, where the endothermic reaction heat requirement dominates, increasing to zero at the "thermal-neutral" voltage, and positive at higher current densities where ohmic heating dominates. Ohmic heating is caused by cell irreversibilities, such as electric and ionic resistance, activation, and concentration polarization. The thermal-neutral voltage can be predicted from direct application of the First Law to the overall system at a specified temperature:

$$Q - W = \dot{N}_{H2} \Delta H_R \tag{5}$$

Letting $Q = 0$ (no external heat transfer), $W=VI$, and noting that the electrical current is directly related to the molar production rate of hydrogen by

$$\dot{N}_{H2} = I / 2F \tag{6}$$

where F is the Faraday number (F = 96,487 J/V mol), yields:

$$V_{tn} = -\Delta H_R / 2F \tag{7}$$

Where V_{tn} is the thermal neutral voltage. The open-cell potential is given by the Nernst Equation, which for the hydrogen/oxygen/steam system takes the form:

$$E = E_o - \frac{RT}{jF} \ln\left[\left(\frac{X_{H2O}}{X_{H2} X_{O2}^{1/2}} \right) \left(\frac{p}{p_{std}} \right)^{-1/2} \right] \tag{8}$$

Activation overpotential due to concentration losses is not included in the FLUENT SOFC module. Mass diffusion within the gas streams is calculated however. For the FLUENT runs,

convergence was deemed acceptable after the continuity residual decreased to lower than 5×10^{-5}, which was generally achieved after about 55 iterations. The continuity residual was chosen since it always has the highest magnitude and is the slowest to converge. FLUENT was run on a double-CPU 2.6-GHz dual core machine running SUSE 10.0 Linux. With a total of 4 cpus run in parallel, each run required about 28 minutes of real time. The model consists of 1.2 million numerical grid cells.

RESULTS

Detailed numerical results for steam utilization, distributions of temperature, mole fraction, and current density and various other results are presented in Table 2 and Figures 4 – 18. Table 2 shows the H_2 and O_2 production rates for various values of cell current. Mass flow rates of H_2 and O_2 for the FLUENT calculations are compared to theoretical values obtained from Faraday's law. These values agree within 0.001% of each other

A base-case total current of 1.5 A, corresponding to a current density of 0.2907 A/cm^2 was used for the contour plots presented in Figures 4 – 11. The corresponding per-cell operating voltage is 1.17 V, which is below thermal neutral. A contour plot of temperatures on the top surface of the ceramic support tube is presented in Figure 4. The black rectangular outlines in Figure 4 represent the locations of the individual cells. The inlet temperature for both the fuel and the air is 1173 K.

Steam/hydrogen enters the domain from the left and air enters from the bottom in cross flow. Minimum temperatures occur in the upper right of the figure, corresponding to the outlet side for both the fuel flow and the air flow. The net cell cooling effect observed for this case is caused by the dominance of the endothermic electrochemical reaction heat requirement at this operating voltage.

Table 2. Hydrogen and Oxygen production rates.

Cell Current	FLUENT $\dot{m}$ O2 Produced	Theoretical $\dot{m}$ O2 Produced	FLUENT $\dot{m}$ H2 Produced	Theoretical $\dot{m}$ H2 Produced
(A)	kg/s	kg/s	kg/s	kg/s
0.50	4.145E-07	4.145E-07	5.223E-08	5.223E-08
1.00	8.291E-07	8.291E-07	1.045E-07	1.045E-07
1.50	1.244E-06	1.244E-06	1.567E-07	1.567E-07
1.98	1.642E-06	1.642E-06	2.069E-07	2.068E-07
2.00	1.658E-06	1.658E-06	2.089E-07	2.089E-07
2.50	2.073E-06	2.073E-06	2.612E-07	2.612E-07

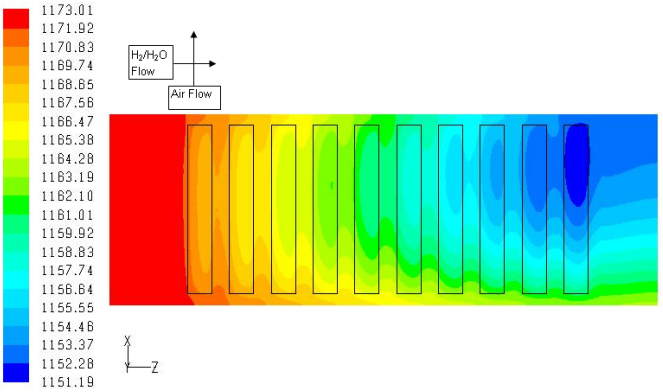

Figure 4. Top view of temperature contours on ceramic tube

Figure 5 shows a front view of the temperature contours cut through the middle of the ceramic tube. For electrolysis, "fuel" signifies H_2O which flows from left to right. Air flow is into the page. For this figure,the vertical height has been magnified 40x to emphasize the variation in the thin x direction. Outlines of the O_2 current collectors can be seen, along with the very thin electrodes and H_2 current collectors. The solid black line cutting across the figure represents the top of the fuel flow channels. As noted in Figure 4, the temperatures are lowest at the trailing edge of the tube.

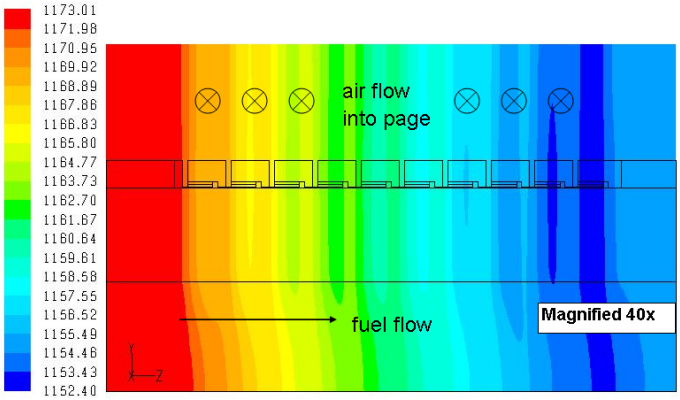

Figure 5. Front view of temperature contours cut through middle of ceramic tube.

Figure 6 shows a top view of the H_2 mole fractions on the top of the ceramic tube. H_2 is being produced and its concentration increases as the flow goes from left to right. All of the cells and most obviously the fifth cell show a high concentration on the trailing edge of each cell. This is due to the relatively high local current density on the trailing edge of each cell as will be discussed later. The second cell shows the variation in the spanwise direction with darker blue dots revealing the locations of the flow channels.

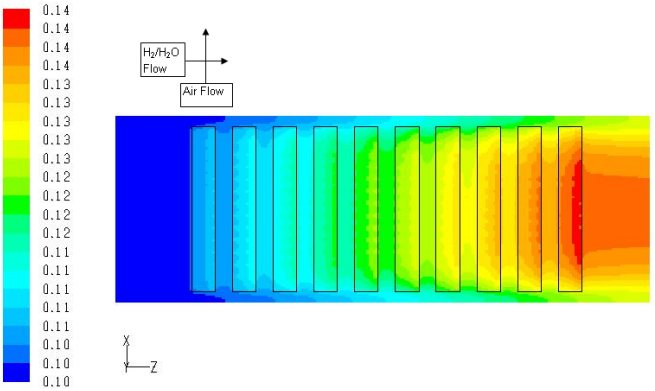

Figure 6. Top view of H_2 mole fractions on ceramic tube.

Figure 7 shows an isometric view of H_2 mole fraction in the flow channels and in the ceramic tube for the base case of -1.5A. The black lines outline the flow channels. H_2O/H_2 enters from the bottom left and exits at the top right. Air flows from the right to the left. Notice from Figure 1 that the tube is 68 mm wide while the active cell area is only 60 mm wide. Hence the outer flow channels (#1 and # 15) are not completely covered by active electrolysis area. This results in a higher H_2O concentration in these outer channels, and hence lower H_2 concentration. The highest H_2 concentrations occur near the electrolyte/electrode interface at the top of each color cutting plane. This is most obvious in the fourth cutting plane. Note that the range of the color bars used in Figures 6 and 7 remained constant for consistency in the two views.

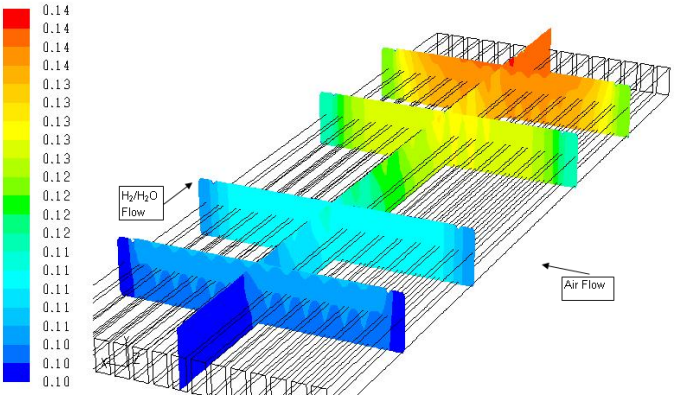

Figure 7. Isometric view of H_2 mole fraction contours in ceramic tube and H_2/H_2O tubes.

Figure 8 shows a top view of the O_2 mole fraction in the air at the top of the computational domain. Air flows from bottom to top in this figure. O_2 is evolved from each active cell area as a result of the electrolysis reaction. The highest O_2 concentrations occur near the downstream end of each cell. The O_2 diffuses into the air as it flows upward and outward. Notice that the minimum mole fraction value indicated in the color bar is 0.21 for O_2 in air, the standard condition.

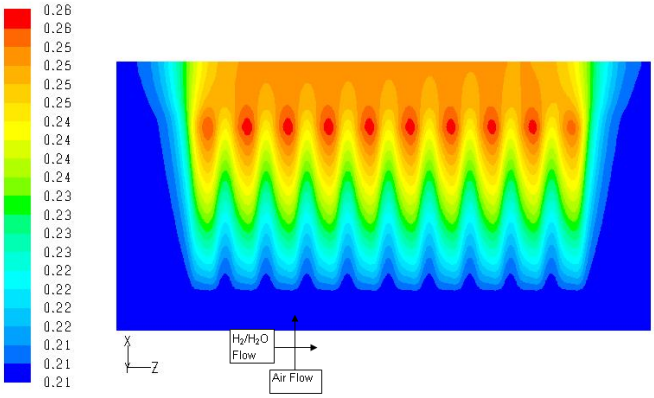

Figure 8. Top view of O_2 mole fraction contours.

Figure 9 shows the top view of the local distribution of Nernst potential for each of the operating cells. As shown in Eqn. 8, the Nernst potential is a strong function of temperature, and mole fraction of H_2O, H_2, and O_2. The temperature and H_2O concentration are lowest at the right side, and the O_2 concentration is highest at the top as discussed about Figure 8. All of these factors contribute to the Nernst potential distribution shown in Figure 9.

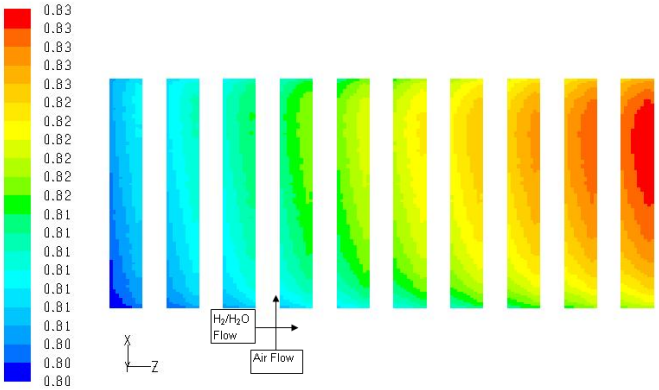

Figure 9. Top view of Nernst potential on electrolytes.

Figure 10 shows the top view of the current density contours in A/m^2 for each electrolyte. Blue values have the highest magnitude of negative current density, and hence the most H_2 production. The highest values of local current density occur at the trailing edge. It is not possible to experimentally measure this phenomenon that the author knows of. Experimentalists might be able to determine that cell degradation occurs at the leading edge because of increased local current density. The specific distribution of current density is sensitive to several factors, including path of least resistance for the segmented-in-series design, magnitude of the activation overpotential, and Nernst potential. Parametric studies have shown that the highest local current densities can be shifted from the trailing edge of the cell to the leading edge of the cell by changing the exchange current density $i_{0,ref}$ and γ in Eqn. 3. This shift can be accomplished by setting $i_{0,ref}$ to a

very large value (1e20), which yields essentially zero activation overpotential, and setting γ=0.5. In a realistic sense, this makes the polarization curve only a function of temperature and concentration and a lot more linear.

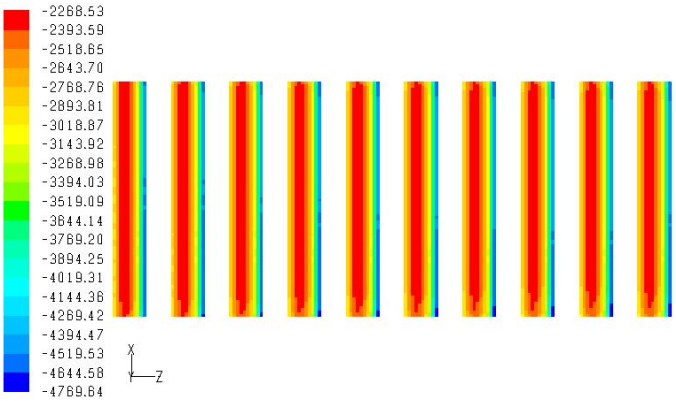

Figure 10. Top view of current density (A/m^2) contours through electrolytes.

Figure 11 presents contours of local activation overpotential in Volts for the base case. These values strongly depend on the specified value of $i_{0,ref}$ in Eqn. 3. Table 1 shows the values used from public literature for $i_{0,ref}$. The largest value of activation overpotential exists on the trailing edge of the cells. This is related to the large current densities at these location (see Eqn. 4).

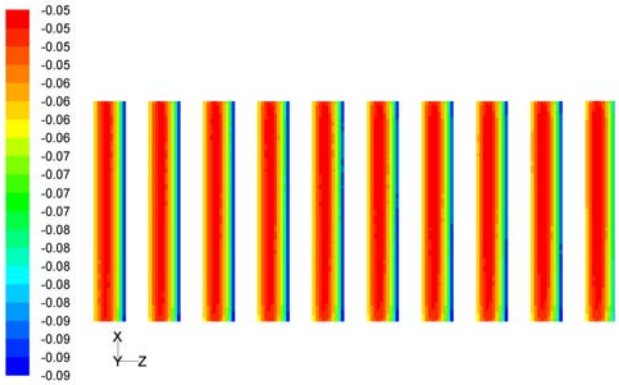

Figure 11. Top view of activation overpotential contours

A polarization curve for this 10-cell electrolysis tube is presented in Figure 12. The curve is fairly linear which denotes relatively little effect of activation overpotential. Future publications will show comparisons with experimental work.

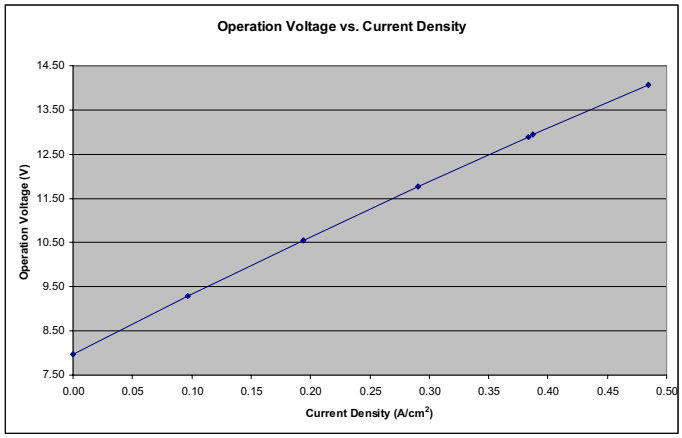

Figure 12. Operating Voltage vs. current density.

Figure 13 presents predicted outlet mole fractions for H_2O, H_2, and O_2 as a function of current density. Equation 6 shows that H_2 production and hence H_2O consumption are directly proportional to the current (and current density). The O_2 mole fraction is not linear, but is shaped like a curve. Because of the low steam utilization specified, it is not obvious on this plot that the O_2 curve is not linear.

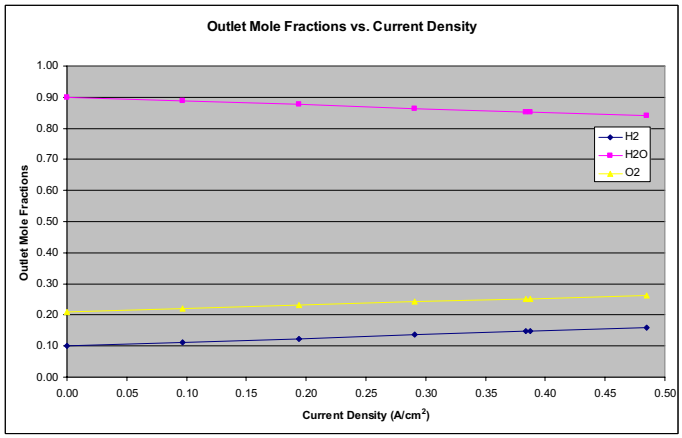

Figure 13. Outlet mole fractions of H_2O/H_2, O_2 for various current densities.

Figure 14 shows the mean outlet gas temperature plotted as a function of operating voltage. The mean outlet gas temperature is calculated by:

$$\overline{T}_{mix,out} = \frac{\sum \dot{m}_i c_{p_i} T_i}{\sum \dot{m}_i c_{p_i}} \qquad (9)$$

The *i* indices in Eqn. 9 indicate the various constituents of H_2O, H_2, O_2, and N_2. The first point on the graph represents the open-cell condition with zero current density and therefore no change in temperature. At higher operating voltages, the endothermic reaction heat requirement causes a decrease in the average outlet gas temperature. Ohmic heating starts to increase the temperature again such that the mean gas

temperature is the same as the inlet temperature at the thermal neutral voltage as calculated from Eqn. 7. This value is 12.946 V (for ten cells) at 1173 K and corresponds to a current of 1.98 A in Figure 12. Previous articles by this author, namely Reference [4] have shown FLUENT to exactly predict the thermal neutral voltage. This IP-SOFC model is off by about 3 degrees. Further investigation will be done by the author to find the reason for this discrepancy.

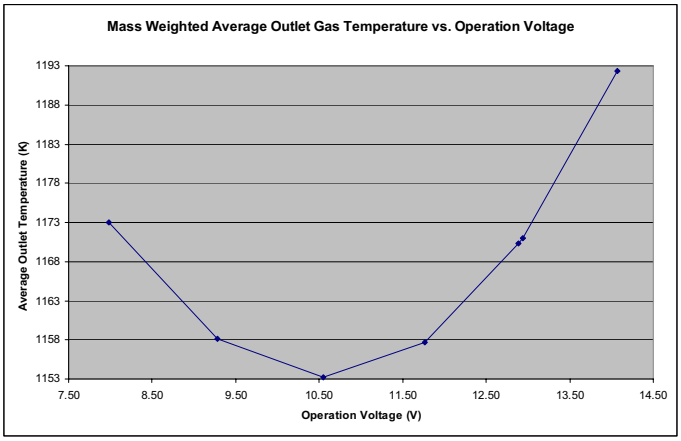

Figure 14. Mass weighted average outlet gas temperatures for various operating voltages.

Figure 15 presents the total volume-average pressure in the H_2 and O_2 electrodes. The mesh considers all of the H_2 and O_2 electrodes to be one element group. During electrolysis, net mass flow occurs from the H_2O/H_2 side to the air side, giving rise to a negative pressure in the H_2 electrode and a positive pressure in the O_2 electrode. Magnitudes are roughly 2% of 1 bar. Previous experience shows that with very high steam utilization (lower flow rates or higher current densities), that these negative pressures in the H_2 electrode can approach 80% of 1 bar. Numerical instability exists when iterations include negative pressure in the Nernst equation and the code fails to converge for these conditions. Both of the curves plotted in Figure 15 are fairly linear. With higher H_2O utilization, the curves have a slight curvature to them. If steam utilization is very high, then steam starvation might occur since the reaction cannot draw enough steam into the reaction area. Also, if the air flow is low, then the O_2 electrodes and O_2 current collector can create high pressures and possibly cause structural damage to the cell such as delamination. These low utilization values in this simulation avoid both of these maladies.

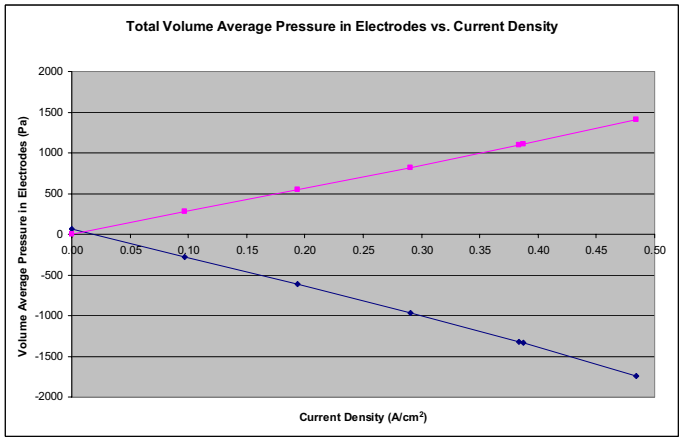

Figure 15. Pressure in electrodes versus current density.

Figure 16 shows the pressure in the H_2 electrode along the tube centerline as a function of axial position for three different current values. Fuel (H_2O) flows from left to right in this plot. Since current density is the highest on the trailing edge as shown in the contour plot of Figure 10, the largest negative pressure occurs in this region also.

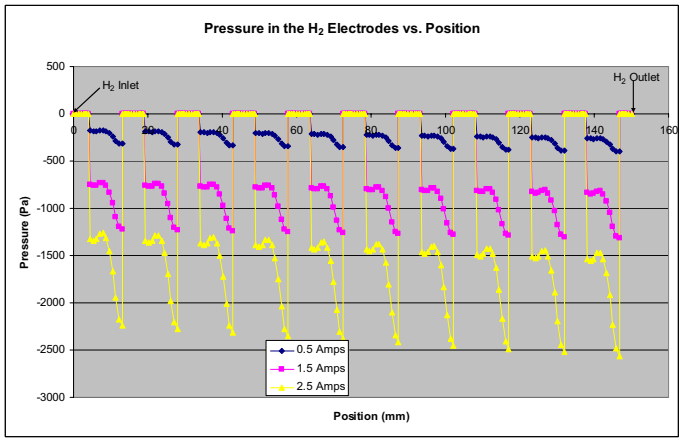

Figure 16. Pressure in electrodes versus position for various currents.

Figure 17 shows the current density through the H_2 electrode along the tube centerline in (A/cm^2) for 0.5, 1.5, and 2.5 Amps. As show in Figure 10, the largest current density magnitudes occur on the trailing edge of the cells and correlates with Figure 16 for largest negative pressure.

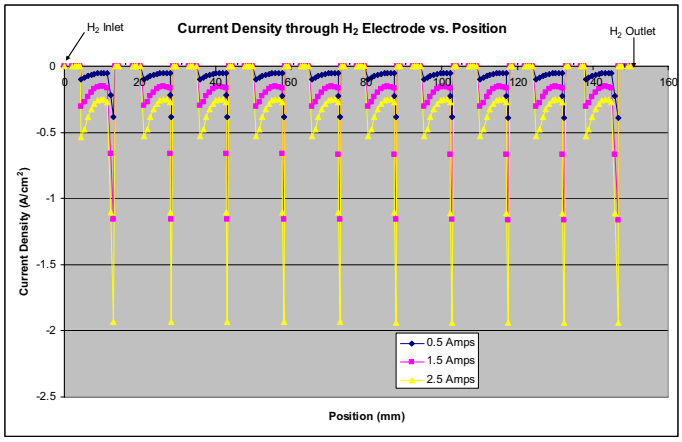

Figure 17. Current density (A/cm^2) through electrolytes for various currents.

Figure 18 shows the average electrolyte temperature for each electrolyte as a function of operating voltage. The leading electrolyte shows the smallest temperature variation, while the last electrolyte (number 10) shows the largest variation in temperature due to the cumulative effect of the upstream cells.

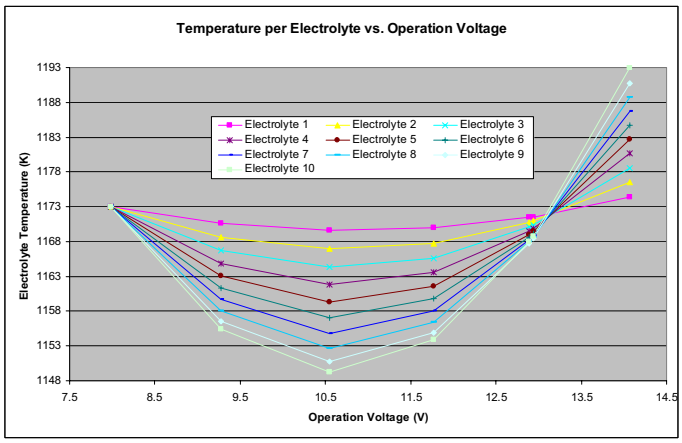

Figure 18. Mean electrolyte temperature for various operating voltages.

CONCLUSIONS

A detailed analysis has been performed with the CFD code FLUENT to predict the performance and operational characteristics of a series of Integrated Planar Solid Oxide Electrolysis Cells (IP-SOEC) deposited on a flattened porous ceramic tube. The FLUENT SOFC module was used to simulate high-temperature steam electrolysis for an IP-SOEC tube with ten cells. A high flow rate of steam/hydrogen was introduced into the model which yields a low value of steam utilization. A high flow rate of air was also introduced. Performance predictions were obtained over a range of cell current values to reveal associated trends in operating voltage, temperature distributions, etc. A polarization curve was created showing a nearly linear V-I correlation.

For the base case, temperature contours in the ceramic tube and printed electrolysis cells showed minimum temperature values near the steam/hydrogen outlet. Mole fractions of H_2 show a maximum near the steam/hydrogen outlet also. Negative pressures were found to be about 2% of 1 bar in the H_2 electrode. Local distributions of Nernst potential, and activation overpotential plots were also discussed. Current density and hence activation overpotential were highest at the trailing edge of the cells. This phenomenon occurred because the activation overpotential parameters were controlled to be able to compare with other codes. There are currently no experimental methods to show that this higher current density and activation overpotential does occur on the leading edge. Visible signs of degradation on the leading edge have not been seen in post examination of experimental tests. O_2 mole fractions were visibly higher on the contour plots where the cells are printed.

Previous high temperature electrolysis models have shown exact agreement with thermal neutral voltage. This IP-SOFC model shows a discrepancy of about 3 degrees K. Future work will include experimental results.

ACKNOWLEDGMENTS

The U.S. Department of Energy, Office of Nuclear Energy, Nuclear Hydrogen Initiative Program supported this work.

COPYRIGHT STATEMENT

REFERENCES

[1] O'Brien, J. E., Stoots, C. M., Herring, J. S., and Hartvigsen, J. J., "Performance of Planar High-Temperature Electrolysis Stacks for Hydrogen Production from Nuclear Energy," *Nuclear Technology*, Vol. 158, pp. 118 - 131, May, 2007.

[2] Herring, J. S., O'Brien, J. E., Stoots, C. M., and Hawkes, G. L., "Progress in High-Temperature Electrolysis for Hydrogen Production using Planar SOFC Technology," *International Journal of Hydrogen Energy*, Vol. 32, Issue 4, pp. 440-450, March 2007.

[3] Hawkes, G. L., O'Brien, J. E., and Stoots, C. M., "3D CFD Model of a Multi-Cell High Temperature

Electrolysis Stack, in review, *International Journal of Hydrogen Energy*, 2008.

[4] Hawkes, G. L., O'Brien, J. E., Stoots, C. M., Herring, J. S., "CFD Model of a Planar Solid Oxide Electrolysis Cell for Hydrogen Production from Nuclear Energy," *Nuclear Technology*, Vol. 158, pp. 132 - 144, May, 2007.

[5] Agnew, G.D., Collins, R.D., Jorger, M., Pyke, S.H., and Travis, R.P., "The Components of a 1MW SOFC System at Rolls-Royce," *Transactions of the ECS*, Volume 7, 2007.

[6] Lai, T. S. and Barnett, S. A., "Effect of cathode sheet resistance on segmented-in-series SOFC power density," *J. Power Sources*, Vol. 164, pp. 742-745, 2007.

[7] Haberman, B. A. and Young J. B., "A Detailed Three-Dimensional Simulation of an IP-SOFC stack," *Journal of Fuel Cell Science and Technology*, Vol. 5, No. 1, 2008.

[8] Haberman, B. A., and Young, J. B., "Three-dimensional simulation of chemically reacting gas flows in the porous support structure of an integrated-planar solid oxide fuel cell," *Int. Journal of Heat and Mass Transfer*, Vol. 47, pp. 3617-3629, 2004.

[9] Hawkes, G. L., O'Brien, J. E., Haberman, B., Marquis, A. J., Martinez Baca, C., Tripepi, D., Costamagna, P., "Numerical Prediction of Performance of Integrated Planar Solid Oxide Fuel Cell, With Comparison of Results from Several Codes," 6th International Fuel Cell Science, Engineering & Technology Conference, paper #65179, June 16-18, 2008, Denver, CO.